Computational and Theoretical Chemistry 1060 (2015) 36–42

Contents lists available at ScienceDirect

Computational and Theoretical Chemistry

journal homepage: www.elsevier.com/locate/comptc

Secondary bonding networks in small $(HgS)_n$ clusters: A theoretical investigation

Hui Cheng, Longjiu Cheng *

Department of Chemistry, Anhui University, Hefei, Auhui 230039, People's Republic of China

ARTICLE INFO

Article history:
Received 21 January 2015
Received in revised form 26 February 2015
Accepted 26 February 2015
Available online 19 March 2015

Keywords:
Mercury sulfide
Genetic algorithm
Global minimum structures
Density functional theory
Secondary bonding

ABSTRACT

Low-lying isomers of mercury sulfide $(HgS)_n$ (n = 2–16, 20) clusters are located by unbiased global search method combining the genetic algorithm with density functional theory. The global minimum structures of mercury sulfide clusters are found to be monotonous rings up to n = 8, and multiple rings at $n \geqslant 9$, and are much different from any other 1:1 clusters. The $(HgS)_n$ clusters have large HOMO–LUMO energy gaps (greater than 3.0 eV at $n \geqslant 3$). S···Hg secondary bonds are found between the rings in multiple-ring structures, where direct evidences for the S···Hg secondary bonding networks are given by noncovalent interaction index analysis. The S···Hg secondary bonding play the key role for the stability of multiple-ring structures, which has a binding energy of about 0.2 eV. Such a secondary bond is due to the strong relativistic effects of Hg and may be the reason for the novel geometric properties of $(HgS)_n$ clusters.

1. Introduction

Semiconductor chalcogenides nanocrystals have attracted extensive interest not only because of their size-dependent characteristic but also because of their novel electronic and optical properties arising out of quantum confinement effects compared with the corresponding bulk compounds [1–10]. **II–VI** semiconductor materials play the central role in many areas of materials of modern science and technology [11–14].

HgS is one of the most important **II–VI** semiconductor compounds possessing excellent optoelectronic properties. It can be widely used in ultrasonic transducers, electrostatic image materials, photoelectric conversion image materials, and photoelectric conversion devices [14]. Generally speaking, bulk HgS consists of cinnabar (hexagonal, red HgS) and meta-cinnabar (cubic, black β-HgS) [15–16].

In recent years, some studies have been done on some binary clusters in ratio of 1:1. Shao et al. [17] reported four types of structures, namely double helical, crown, catenane, and separate rings for $(AuSR)_n$. The catenane structure becomes the most stable at n = 10–12, followed by the double helical and crown structures. For $(ZnS)_n$ [18–24], $(ZnO)_n$ [25–29], $(BeO)_n$ [30] and $(BN)_n$ [31–40] clusters, the structures are rings and cages. Earlier studies have shown that the most stable structure for $(ZnS)_n$ clusters with n = 10–47 are hollow polyhedral clusters [19]. For $(BeO)_n$ clusters, the global minimum (GM) structures are rings to n = 5, double rings at n = 6 and 7, and cages at $n \geqslant 8$ [30]. For $(MgO)_n$ [41–51], $(TiO)_n$ [52] and $(BaO)_n$ clusters [53], the structures are preferred over the cubic-like ones. Puente and Aguado [44] showed that the interpretation of the magic numbers of small $(MgO)_n$ clusters in terms of stacking small $(MgO)_3$ subunits is cube. There are many specific cluster size (n = 4, 5, 8) where the cubic-like structures have the lowest energy of $(TiO)_n$ clusters [52].

In this article, we adopted density functional theory (DFT) method combined with genetic algorithm to predict the structures of $(HgS)_n$ clusters at n = 2–14. Based on the geometric knowledge at small size, putative structures at n = 15, 16, 20 were constructed. The results show that the GM structures are monotonous rings at n = 2–8 and multiple-ring structures at n = 9–16, 20. The geometric structures of $(HgS)_n$ clusters are very unique and different from any other clusters. Moreover, we found that the S···Hg secondary bonding play the key role for the stability of the multiple-ring clusters. Similar to hydrogen bond and halogen bond, the S···Hg secondary bond is also a kind of noncovalent interaction, which is weaker than covalent bond but is much stronger than van der Waals (VDW) interactions. Such a secondary bond may be due to the strong relativistic effects of Hg.

2. Computational details

In this work, the TPSSh functional [54] was selected in DFT calculations, which has been proven reliable for $(AuSR)_n$ clusters compared to experiments [55].

* Corresponding author.
E-mail address: clj@ustc.edu (L. Cheng).

http://dx.doi.org/10.1016/j.comptc.2015.02.020
2210-271X/

The low-energy isomers of $(HgS)_n$ (n = 2–14) clusters were located by two ways. One is by starting from the low-energy isomers of $(ZnS)_n$ [18–24], $(BeO)_n$ [30], $(MgO)_n$ [41–51] and $(AuSR)_n$ [17] clusters as reported in literatures. The other is by unbiased global search by the combination of genetic algorithm (GA) and DFT method, which has been successfully applied in the structural prediction of a number of systems [30,56–61]. GA is a search heuristic that mimics the process of natural selection. This heuristic is routinely used to generate useful solutions to optimization and search problems. GA belongs to the larger class of evolutionary algorithms, which generate solutions to optimization problems using techniques inspired by natural evolution, such as inheritance, mutation, selection, and crossover.

In GA-DFT procedure, small basis sets (6-31G* [62] for S and LANL2DZ [63] for Hg) are selected for saving time to perform unbiased search of the potential energy surface. The structures of $(HgS)_n$ (n = 15, 16, 20) cluster were constructed based on the geometric structures of small $(HgS)_n$ clusters. After global optimization, the low-lying isomers were fully relaxed with larger basis sets (6-311G* [64] for S and def2-TZVP [65] for Hg). For Hg, we used a 19-valence-electron scalar relativistic pseudopotentials together with the corresponding (8s8p6d1f)/[6s4p3d1f] valence basis set [66]. The energies and HOMO–LUMO gaps are also obtained at TPSSh/6-311G*/def2-TZVP level of theory. All calculations are carried out using the GAUSSIAN 09 package [67].

3. Results and discussion

Combining the GA with DFT method, we obtained a series of structures for $(HgS)_n$ (n = 2–14) clusters at TPSSh/6-311G*/def2-TZVP level. All putative GM structures of $(HgS)_n$ clusters at n = 2–14 were located in GA-DFT unbiased search. For comparison, some typical GM structures of $(BeO)_n$, $(ZnS)_n$, and $(AuSR)_n$ clusters in literatures were also optimized. For larger sizes, n = 15, 16 and 20, it is very difficult for unbiased global search using GA-DFT method, and some typical structures were modeled based on the geometric structures of small clusters. The isomers of $(HgS)_n$ (n = 2–8) and $(HgS)_n$ (n = 9–16, 20) clusters are plotted in Fig. 1 and Fig. 2, respectively. Both the three lowest-energy isomers and the isomers with typical motifs, which may be the GM structures of some other clusters, are plotted. The plotted isomers are either top 3 lowest-energy All the isomers are verified to be true local minima by frequency check. The GM structures are monotonous rings up to n = 8, and multiple rings at n = 9–16, 20.

3.1. Geometry structures

$(HgS)_n$ (n = 2–8). The GM structure of $(HgS)_2$ is a rhombus (2**I**, D_{2h}) with bond length of Hg–S = 2.50 Å and bond angle of S–Hg–S = 111.1°. The structure is 0.25 eV lower than the V-shaped configuration (2**II**). The lowest-energy structure of $(HgS)_3$ is a triangular ring (3**I**, D_{3h}) with bond length of Hg–S = 2.39 Å and bond angle of S–Hg–S = 158.8°, which is also the most stable structure of $(ZnO)_3$ cluster [28]. The lowest energy configuration found for $(HgS)_4$ is a square ring (4**I**, D_{2d}) with bond length of Hg–S = 2.36 Å and bond angle of S–Hg–S = 177.9°, which is 3.27 eV more stable than the cage structure 4**II** (T_d). A monotonous ring structure is obtained for $(HgS)_5$ (5**I**, C_s) as the lowest energy structure. 5**I** and 5**II**(C_2) in helix have nearly equal energy. 5**III** with a 4-membered ring and one tail (Hg–S). For $(HgS)_6$, a crown monotonous ring (6**I**, D_{3d}) is found to be most stable. 6**I** is only 0.05 eV more stable than a helix (6**II**, D_2). 6**III** (D_{3d}) with two 3-membered rings is much less stable than 6**I**. A monotonous ring of $(HgS)_7$ (7**I**, C_2) was found to be the most stable structure. 7**II** (C_2) with a helix is less stable than 7**I** by only 0.02 eV, where such a helix structure was also found for

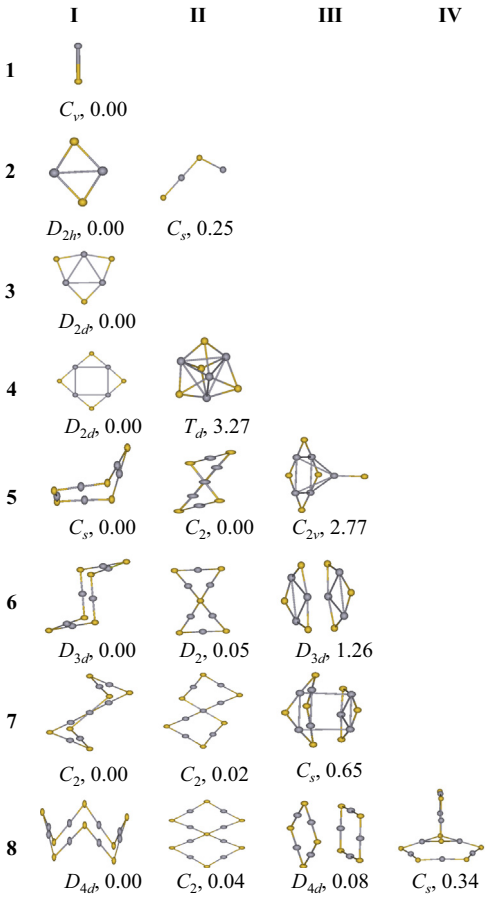

Fig. 1. The global minimum and low-energy isomers for $(HgS)_n$ (n = 1–8) clusters at the TPSSh/6-311G*/def2-TZVP level. The structures in column **I** correspond to the global minima; columns **II**–**IV** correspond to isomers (local minima) that are higher in energy, and the symmetry and the relative energies in eV are labeled in figure. Hg-gray, S-yellow. (For interpretation of the references to colour in this figure legend, the reader is referred to the web version of this article.)

$(AuSR)_7$ [17]. 7**III** (C_s) consists of a 4-membered ring and a 3-membered ring. A crown is obtained for $(HgS)_8$ (8**I**, D_{4d}) as the lowest-energy structure. 8**II** (C_2), in similar helix structure with $(AuSR)_8$ [17], is only 0.04 eV higher in energy than 8**I**. 8**III** (D_{4d}) consists of two 4-membered rings with high symmetry.

$(HgS)_n$ (n = 9–14). For $(HgS)_9$, a double-ring structure (9**I**, C_1) is the most stable isomer. The second isomer has a helix structure (9**II**, C_2), which is the most stable structure of $(AuSR)_9$ [17]. 9**III** (C_3) consists of 3**I** and 6**I**. A C_{2v} isomer (9**IV**) and a D_{3h} isomer (9**V**) are 1.01, 1.65 eV higher in energy, respectively. The most stable structure of $(HgS)_{10}$ (10**I**, C_{2v}) consists of two 5-membered rings. The second low-lying isomer (10**II**) is in D_{5d} symmetry. 10**III** (C_s), which consists of a 4-membered ring and a 6-membered ring, and 10**IV**(D_{5d}, crown) are nearly identical in energy**.** The catenane structure 10**V**(D_2), known as GM structure of $(AuSR)_{10}$, is 1.09 eV higher in energy than 10**I**. For $(HgS)_{11}$, 11**I** (C_s) which consists of a 7-membered ring (chair like) and a 4-membered ring is most stable. 11**IV** with C_2 symmetry is the most stable configuration of $(AuSR)_{11}$. The GM structure 12**I** consists of a 4-membered ring and a 8-membered ring (crown) with C_{4v} symmetry. 12**II** (D_{3d}) consists of two 6**I** (6-membered ring). 12**III** (D_{4h}) consists of three 4-membered rings. 12**IV** (D_{6d}) is a crown structure. 12**V** (C_2) has similar structure with the most stable structure of $(AuSR)_{12}$. 12**VI** (T_h) is the most stable structure of ZnO [28] and BeO [30] and is 1.27 eV higher in energy than 12**I**. For $(HgS)_{13}$, 13**I**(C_s) consists of a 5-membered ring (5**I**) and a 8-membered ring

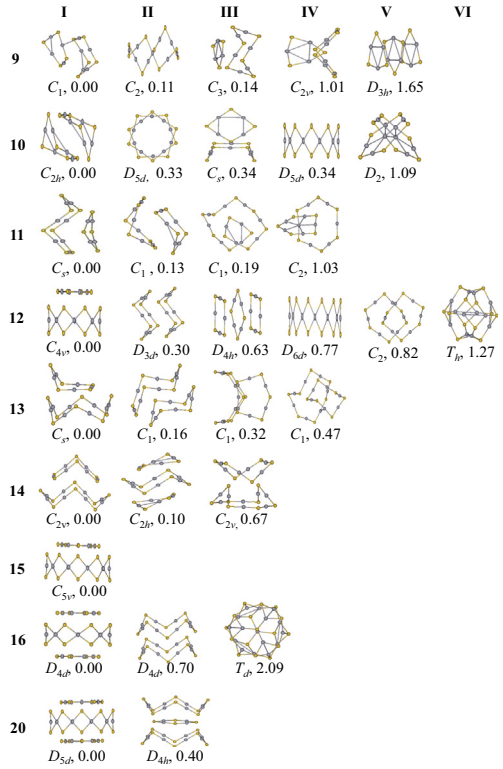

Fig. 2. The global minimum and low-energy isomer for $(HgS)_n$ (n = 9–16, 20) clusters at the TPSSh/6-311G*/def2-TZVP level. Hg-gray, S-yellow. (For interpretation of the references to colour in this figure legend, the reader is referred to the web version of this article.)

(8**I**, crown). 13**II** (C_1) and 13**III** (C_1) are both double-ring structures. The catenane 13**IV** with C_1 symmetry is 0.47 eV higher in energy than 13**I**. The lowest-energy configuration of $(HgS)_{14}$ is 14**I** in C_{2v} symmetry, which consists of a 6-membered ring and a 8-membered ring (8**I**, crown). 14**II** (C_{2h}) is a triple-ring structure and 14**III** (C_{2v}) is a double-ring structure.

$(HgS)_n$ (n = 15, 16, 20). For $(HgS)_{15}$, 15**I** which consists of a 5-membered ring and a 10-membered ring (crown) is in C_{5v} symmetry. The most stable structure for $(HgS)_{16}$ with D_{4d} symmetry consists of two 4-membered rings and a 8-membered ring (crown). 16**II** in D_{4d} symmetry is 0.70 eV higher in energy than 16**I**, which consists of two 8-membered rings (8**I**, crown). 16**III** (T_d) is the most stable structure of $(ZnO)_{16}$ [25,27,28] and is 2.09 eV higher in energy than 16**I**. For $(HgS)_{20}$, 20**I** consists of two 5-membered rings and a 10-membered ring (crown) in D_{5d} symmetry. 20**II**, which consists of one 4-membered ring and two 8-membered rings, is 0.40 eV less stable than 20**I**.

3.2. Stability

The energy gap (E_{HL}) between the highest occupied molecular orbital (HOMO) and lowest unoccupied molecular orbital (LUMO) is an important factor of the stability. As shown in Fig. 3a, the $(HgS)_n$ clusters have large HOMO–LUMO energy gaps (greater than 3.0 eV at $n \geqslant 3$), indicating high electronic stability. The E_{HL} increases with cluster size increasing and reaches the maximum at n = 6. It is because the small rings are strained in geometric structure, and the release of the strains increases the E_{HL} value. There is an odd–even effect in energy gaps at n = 6–8. At $n \geqslant 9$, gaps of the multiple rings are obvious lower than those of monotonous rings at n = 6–8, because there are small rings ($n \leqslant 5$) in the multiple-ring clusters.

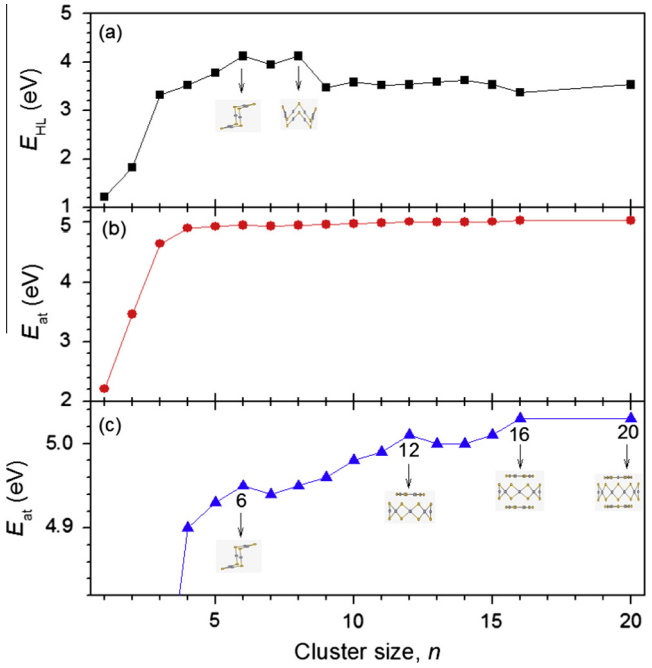

Fig. 3. (a) The energy gap E_{HL} of the global minima of $(HgS)_n$ (n = 1–16, 20) as a function of the cluster size n. (b) Atomization energy per HgS unit (E_{at}) of the global minima as a function of the number of HgS units n. (c) Enlarged atomization energy per HgS unit (E_{at}) of the global minima in 4.82–5.05 eV region.

The average atomization energy (E_{at}) of the $(HgS)_n$ clusters is defined as the average binding energy per HgS unit: $[n * E(Hg) + n * E(S) - E(HgS)_n]/n$. Fig. 3b and c plot the E_{at} of the most stable structures of $(HgS)_n$ as a function of cluster size. It can be seen that E_{at} increases rapidly with cluster size increasing at $n \leqslant 4$, and changes little at $n \geqslant 5$. The E_{at} of n = 6 is the highest in the monotonous rings, and the E_{at} of n = 12, 16, 20 are higher than other clusters in multiple-ring structures, as a consequence of the stability of their geometric structures.

3.3. Secondary bonding

For $n \geqslant 9$, the multiple-ring structures are more stable than other structures, and these multiple-ring structures are much different from any other 1:1 clusters. We infer that the stability of multiple-ring structures may due to the secondary bonds in those structures. The structure of many main group compounds often reveal short distances between a heavy p-block element and one or more atoms which possess lone pair of electrons. The distance cannot be dismissed as "non-bonded interactions" [68]. Alcock used the term "Secondary bonding interactions" in 1970 for these types of interactions [69,70].

Here we select 10**I** and 10**II** as examples to illustrate the difference of S···Hg secondary bond and the coulomb interactions between S and Hg. As we know, S is partially negative charge and Hg is partially positive charge in $(HgS)_n$ clusters. 10**II** is the optimal double-ring motif for coulomb interactions, which has the maximum nearest-neighbor coulomb interactions. However, 10**II** is even 0.33 eV higher in energy than another double-ring structure (10**I**). Fig. 4 compares the geometric structures of 10**I** and 10**II** in detail. It is found that S–Hg bond lengths in these two structures are nearly identical (~2.35 Å), and the 10 nearest-neighbor coulomb distances in 10**II** are 3.56 Å. Interestingly, there are two S···Hg interactions between the two rings in 10**I** with distances 3.19 Å, which is 0.84 Å longer than S–Hg bond and 0.37 Å shorter than coulomb distance. Thus, we infer that these

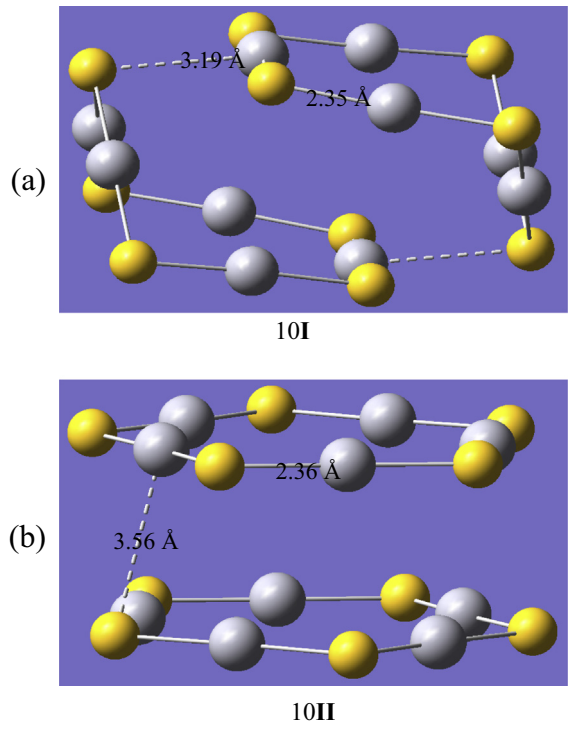

Fig. 4. (a) Secondary bonding patterns for 10**I**; (b) Coulomb interaction patterns for 10**II**. Hg-gray, S-yellow. (For interpretation of the references to colour in this figure legend, the reader is referred to the web version of this article.)

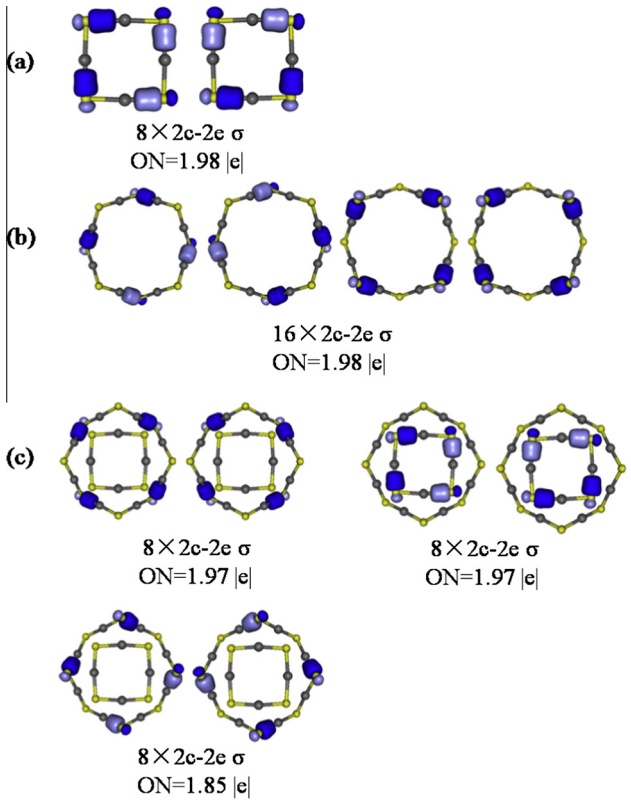

Fig. 6. (a) AdNDP localized bonding patterns of structure 4**I**; (b) AdNDP localized bonding patterns of structure 8**I**; (c) AdNDP localized bonding patterns of structure 12**I**. ON corresponds to the occupancy number; 2c–2e (two-center two-electron).

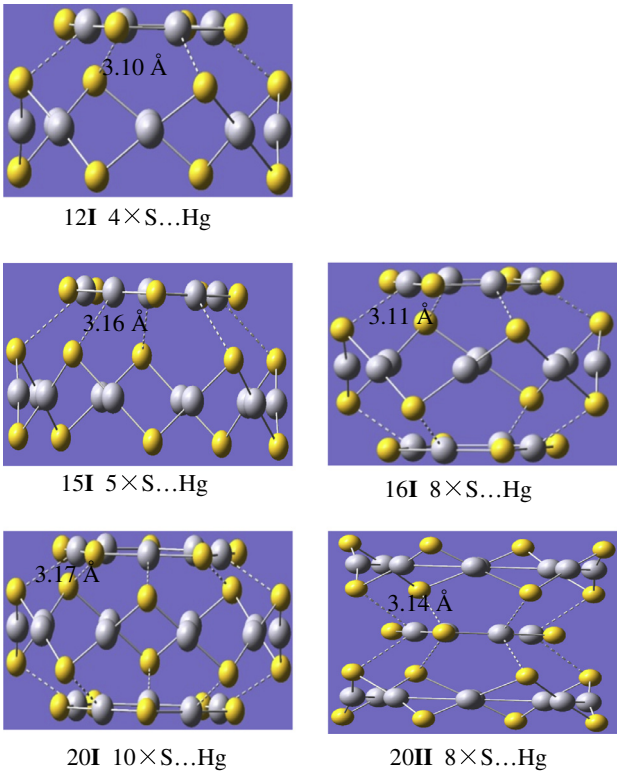

Fig. 5. Secondary bonding patterns of 12**I**, 15**I**, 16**I**, 20**I**, 20**II**. S-yellow, Hg-gray. (For interpretation of the references to colour in this figure legend, the reader is referred to the web version of this article.)

two S···Hg interactions should be secondary bonding interactions, and such a secondary bond is the reason why 10 **I** is more stable than 10**II**.

In Fig. 5, some typical structures with S···Hg secondary bonds (12**I**, 15**I**, 16**I**, 20**I**, 20**II**) are plotted. The S···Hg distances of those clusters are about 3.10–3.17 Å. There are 4 S···Hg secondary bonds between the 8-membered and 4-membered rings in 12**I**. 15**I** with a 10-membered ring and a 5-membered ring structure includes 5 S···Hg secondary bonds. There are 8 S···Hg secondary bonds in 16**I** between the central 8-membered ring and two 4-membered rings in both sides. Similarly, there are 10 S···Hg secondary bonds in 20**I** and 8 S···Hg secondary bonds in 20**II**.

As we know, the bonding energy of one hydrogen bond (O···H secondary bond) is nearly 0.20 eV [66,67]. 12**I** consists of $(HgS)_8$ and $(HgS)_4$ and has four S···Hg secondary bonds, so the interaction energy of each S···Hg secondary bond can be roughly calculated $E(S\cdots Hg) = [E(HgS)_8 + E(HgS)_4 - E(HgS)_{12}]/4$. The calculated $E(S\cdots Hg)$ in 12**I**, 15**I**, 16**I**, 20**I**, 20**II** are 0.23, 0.18, 0.23, 0.18, 0.20 eV, respectively, which are obviously in the energy level of hydrogen bonds. As a comparison, the coulomb interaction in 10**II** is calculated to be only 0.02 eV (the calculated natural charges for S and Hg are −0.82|e| and +0.82|e|, respectively). For $(HgS)_{20}$, in the geometric structures part, we introduced that 20**I** is 0.40 eV more stable than 20**II**. And the S···Hg secondary bonds in 20**I** are two more than those in 20**II**. The two more S···Hg secondary bonds result in about 0.40 eV lower energy of 20**I**.

The bonding pattern of HgS clusters is very clear. Each Hg atom, which is in *sp* hybridization, is bonded with two S atoms with S–Hg–S angle about 180°. Similarly, S atom is in sp^3 hybridization linked by two Hg atoms, and the Hg–S–Hg angle is about 100°. To gain direct insight into the nature of bonding of $(HgS)_n$ clusters, we apply a tool named adaptive natural density partitioning (AdNDP)

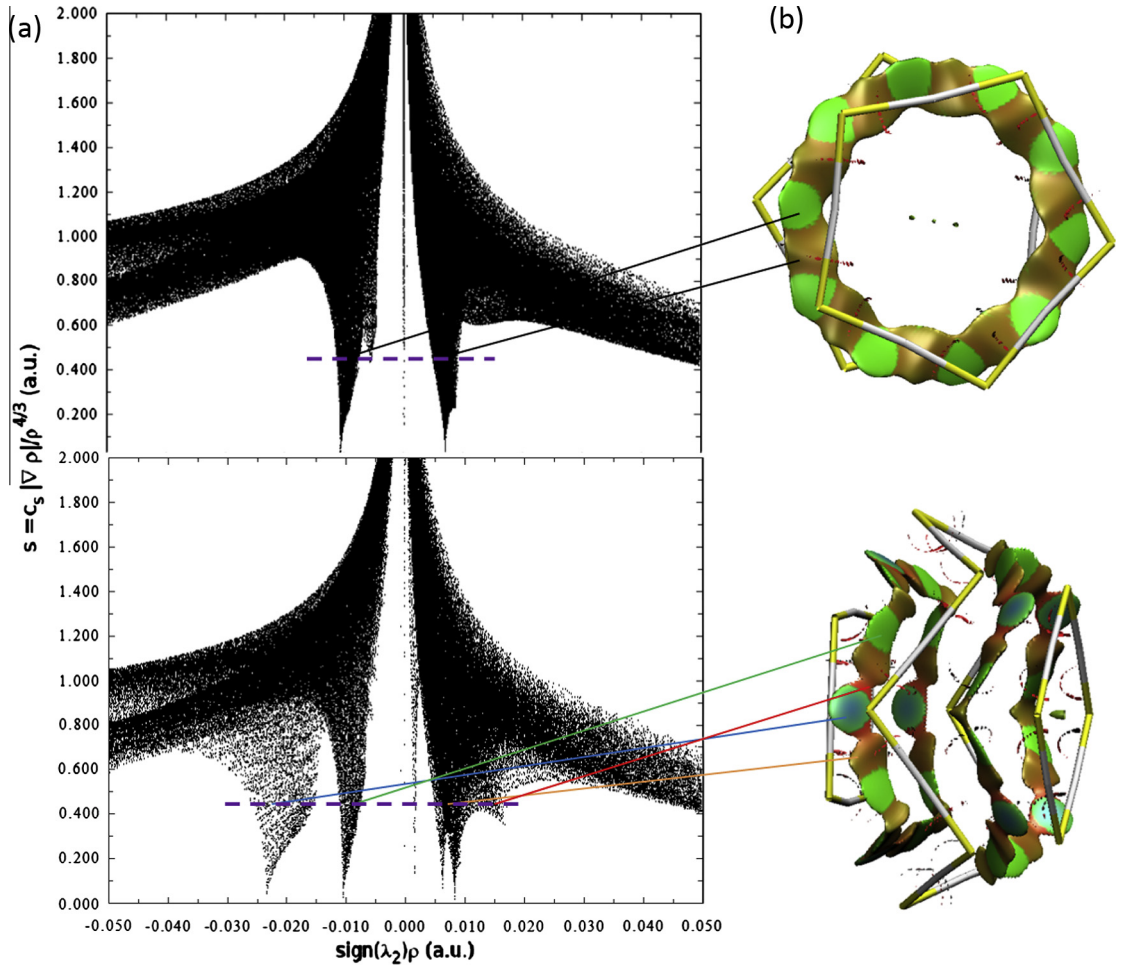

Fig. 7. (a) Plots of the reduced density gradient versus the electron density multiplied by the sign of the second Hessian eigenvalue, and (b) NCI isosurfaces (s = 0.45) for 10**II** (top) and 16**I** (bottom).

[71–73] to obtain patterns of chemical bonding. 4**I** is an octagonal ring, 8**I** is a crown and 12**I** consists of 4**I** and 8**I**. Therefore we analyze the chemical bonding of 4**I**, 8**I** and 12**I**by using AdNDP as plotted in Fig. 6.

According to AdNDP analysis, 4**I** contains eight two-center two-electron (2c–2e) σ-HgS bonds with occupancy number ON = 1.98|e| close to the ideal limit of 2.00|e| (Fig. 6a). Similarly, 8**I** includes sixteen Hg–S σ bonds with same occupancy numbers ON = 1.98|e| (Fig. 6b). As expected, the AdNDP bonding shows that 12**I** can be viewed as two separated parts (4**I** and 8**I**) without covalent interactions. However, for the eight Hg–S bonds with S atoms involved in the S···Hg secondary bonds, the ONs are only 1.85|e| (Fig. 6c). From AdNDP analysis, the S···Hg secondary bonds cannot be viewed directly, but the low ONs of HgS bonds involved in S···Hg secondary bonds may indicate certain non-Lewis interaction.

The secondary bonding is a kind of non-Lewis/noncovalent interaction and cannot be studied directly by the natural bonding orbital methods such as AdNDP. Recently, Yang group [74,75] developed a noncovalent interaction (NCI) index approach to detect noncovalent interactions based on the electron density and its derivatives. NCI index provides a rich representation of VDW interactions, hydrogen bonds, and steric repulsion. The definition of NCI index is based on the reduced density gradient, s, and the electron density, ρ, where

$$s = \frac{1}{2(3\pi^2)^{1/3}} \frac{|\nabla\rho|}{\rho^{4/3}}.$$

and which permits to highlight interactions characterized by a low-density regime. The bonded and nonbonded interactions can then be identified by the sign of the second Hessian eigenvalue (λ_2), whereas the density itself provides information about their strength.

Fig. 7a plots the reduced density gradient (s) versus the electron density (ρ) multiplied by the sign of λ_2 of the two typical structures 10**II** and 16**I**. The low-density regime represents noncovalent/weak interactions. In the data of 10**II**, the low density, low-gradient spike lying at negative values indicates stabilizing weak interactions (nearest neighbor SHg coulomb attraction between the two rings), and the spike at positive values represents unstabilizing weak interactions (nearest neighbor SS and HgHg coulomb repulsion between the two rings). There are corresponding coulomb SHg, SS and HgHg interactions in the data of 16**I** as in 10**II**. However, there is a low-gradient spike lying at about sign (λ_2) $\rho = -0.025$ au in the data of 16**I** similar to that in water dimer, which represents strong stabilizing noncovalent interactions (S···Hg secondary bonding). Fig. 7b displays low-gradient (s = 0.45 au) NCI isosurfaces, subject to the constraint of low density, for 10**II** and 16**I**. The gradient isosurfaces are colored according to the corresponding values of sign (λ_2)ρ, which is a good indicator of interaction strength. The gradient isosurfaces provide a rich

visualization of noncovalent interactions as broad regions of real space, where the coulomb attracting (green), coulomb repulsion (brown), S···Hg secondary bonding (blue) and steric repulsion (red) are viewed directly. The NCI studies are carried out using Multiwfn package [76], and the NCI isosurface images are created using VMD [77].

3.4. Relativistic effects

Au has the largest relativistic effects in all elements [78–79], which results in novel geometric structures of $(AuSR)_n$ clusters. Hg also has reasonable large relativistic effects [80], and $(HgS)_n$ is binary clusters in ratio of 1:1 the same as $(AuSR)_n$. However, there are great differences between geometries of $(HgS)_n$ and $(AuSR)_n$ clusters. $(AuSR)_n$ clusters favor catenane structures. Schmidbaur and co-workers [81–83] investigated that the mechanism of the surprisingly facile catenane formation can be assumed to include various intermediates with different forms of aurophilicity interactions which lower the activation barriers of significant steps of the reactions. However, for $(HgS)_n$ clusters, the multiple-ring structures are found to be stable for large size. It is clearly seen that the S···Hg secondary bonds in isomers play the key role for the stability of the multiple-ring structures.

$(ZnS)_n$ clusters [18,19] favor cage-like structures, and are much different from those of $(HgS)_n$ clusters, where the reason for the difference is suggested to be the relativistic effects. To verity the relativistic effects in $(HgS)_n$ clusters, we compared the energy of 12**I** and 12**VI** using the Sttutgart–Dresden non-relativistic pseudopotentials [84], where the cage-like 12**VI** is the lowest-energy structure of $(ZnS)_{12}$ cluster [19]. Interestingly, for $(HgS)_{12}$ cluster, the cage-like 12**VI** is calculated to be even 1.87 eV lower in energy than 12**I** using the non-relativistic pseudopotentials, which indicates that the relativistic effects lead to the special S···Hg secondary bonding in HgS clusters.

4. Conclusions

In summary, we predicted the geometric structures of $(HgS)_n$ (n = 2–16, 20) clusters using DFT calculations. The GM structures are monotonous rings at n = 2–8 and multiple rings at $n \geqslant 9$. $(HgS)_n$ clusters have large HOMO–LUMO energy gaps (greater than 3.0 eV at $n \geqslant 3$) indicating high electronic stability. By analyzing the bonding energy and distances, it is found that the multiple-ring structures are stabled by the networks of S···Hg secondary bonds. The calculated distance of the S···Hg secondary bond is about 3.1 Å (0.84 Å longer than S–Hg bond distance and 0.37 Å shorter than coulomb distance) and the energy level is about 0.2 eV. Moreover, direct evidences of the S···Hg secondary bonding networks in the multiple-ring structures are given by noncovalent interaction index analysis. The geometric structures of $(HgS)_n$ clusters are much different from those of $(ZnS)_n$ clusters due to the relativistic effects, where the later favor cage-like structures. However, the non-relativistic calculations show that $(HgS)_{12}$ cluster also favors cage-like structure. Strong relativistic effects lies in both $(HgS)_n$ and $(AuSR)_n$ clusters, but leads to different results: secondary bonding networks and aurophilicity interactions.

Acknowledgements

This work is financed by the National Natural Science Foundation of China (NNSFC) (21273008), and by the 211 project of Anhui University. The calculations were carried out at the High-Performance Computing Center of Anhui University.

References

[1] J.M. Azpiroz, I. Infante, X. Lopez, J.M. Ugalde, F. De Angelis, A first-principles study of II–VI (II = Zn; VI = O, S, Se, Te) semiconductor nanostructures, J. Mater. Chem. 22 (2012) 21453–21465.
[2] P. Chiquet, P. Masson, J. Postel-Pellerin, R. Laffont, G. Micolau, F. Lalande, A. Regnier, Experimental setup for non-destructive measurement of tunneling currents in semiconductor devices, Measurement 54 (2014) 234–240.
[3] D. Dirin, S. Dreyfuss, M. Bodnarchuk, G. Nedelcu, P. Papagiorgis, G. Itskos, M. Kovalenko, Lead halide perovskites and other metal halide complexes as inorganic capping ligands for colloidal nanocrystals, J. Am. Chem. Soc. 136 (2014) 6550–6553.
[4] Z. Li, Q. Sun, X. Yao, Z. Zhu, G. Lu, Semiconductor nanowires for thermoelectrics, J. Mater. Chem. 22 (2012) 22821–22831.
[5] A. Marzouki, J. Mimila, M. Oueslati, J.M. Laroche, F. Jomard, A. Lusson, P. Galtier, V. Sallet, Electrical and optical studies of metal organic chemical vapor deposition grown N-doped ZnO films, J. Vac. Sci. Technol., B 27 (2009) 1705–1709.
[6] T. Minami, T. Miyata, Y. Nishi, Cu_2O-based heterojunction solar cells with an Al-doped ZnO/oxide semiconductor/thermally oxidized Cu_2O sheet structure, Sol. Energy 105 (2014) 206–217.
[7] M. Qiu, Z. Liu, Z. Tian, W. Wang, Y. Huang, Study of unidirectional conductivity on the electrical discharge machining of semiconductor crystals, Prec. Eng. 37 (2013) 902–907.
[8] T. Sahoo, J. Choi, J. Yoo, Y. Yu, S. Jeon, J. Baek, H. Yoon, S. Hwang, I. Lee, Hydrothermal growth of ZnO nanorods on a-plane GaN/sapphire template, J. Cryst. Growth 312 (2010) 2857–2860.
[9] Z. Pan, L. Chen, G. Chen, Testing of defects in Si semiconductor apparatus by using single-photon detection, Nucl. Instrum. Methods B 307 (2013) 210–213.
[10] X. Zong, L. Wang, Ion-exchangeable semiconductor materials for visible light-induced photocatalysis, J. Photochem. Photobiol., C 18 (2014) 32–49.
[11] I. Mukherjee, S. Senapati, D. Mitra, A. Rakshit, A. Das, S. Moulik, Physicochemistry of dispersions of HgO, HgS and 'Makardhwaj' (an Ayurvedic medicine) prepared in micelle and microemulsion templates, Colloids Surf. A 360 (2010) 142–149.
[12] M. Ozaki, M. Uddin, E. Sasaoka, S. Wu, Temperature programmed decomposition desorption of the mercury species over spent iron-based sorbents for mercury removal from coal derived fuel gas, Fuel 87 (2008) 3610–3615.
[13] W. Xu, S. Lou, S. Li, H. Wang, H. Shen, J. Niu, Z. Du, L. Li, Moderate temperature synthesis of flower- and dot-shaped HgS nanocrystals, Colloids Surf. A 341 (2009) 68–72.
[14] L. Zhang, G. Yang, G. He, L. Wang, Q. Liu, Q. Zhang, D. Qin, Synthesis of HgS nanocrystals in the Lysozyme aqueous solution through biomimetic method, Appl. Surf. Sci. 258 (2012) 8185–8191.
[15] S. Biering, A. Hermann, J. Furthmuller, P. Schwerdtfeger, The unusual solid-state structure of mercury oxide: relativistic density functional calculations for the group 12 oxides ZnO, CdO, and HgO, J. Phys. Chem. A 113 (2009) 12427–12432.
[16] S. Biering, P. Schwerdtfeger, A comparative density functional study of the low pressure phases of solid ZnX, CdX, and HgX: trends and relativistic effects, J. Chem. Phys. 136 (2012) 034504.
[17] N. Shao, Y. Pei, Y. Gao, X. Zeng, Onset of double helical structure in small-sized homoleptic gold thiolate clusters, J. Phys. Chem. A 113 (2009) 629–632.
[18] S. Hamad, C. Catlow, Computational study of the relative stabilities of ZnS clusters, for sizes between 1 and 4 nm, J. Cryst. Growth 294 (2006) 2–8.
[19] S. Hamad, C. Catlow, E. Spano, E. Matxain, J. Ugalde, Structure and properties of ZnS nanoclusters, J. Phys. Chem. B 109 (2005) 2703–2709.
[20] A. Mohajeri, M. Alipour, M. Ahmadi, A graph theory study on $(ZnS)_n$ (n = 3–10) nanoclusters, Chem. Phys. Lett. 503 (2011) 162–166.
[21] S. Pal, B. Goswami, P. Sarkar, Size-dependent properties of ZnS clusters: a density-functional tight-binding study, J. Chem. Phys. 123 (2005) 044311.
[22] S. Pal, R. Sharma, B. Goswami, P. Sarkar, S. Bhattacharyya, A search for lowest energy structures of ZnS quantum dots: genetic algorithm tight-binding study, J. Chem. Phys. 130 (2009) 214703.
[23] E. Spano, S. Hamad, C. Catlow, ZnS bubble clusters with onion-like structures, Chem. Commun. 27 (2004) 864–865.
[24] X. Zhang, M. Zhao, T. He, W. Li, X. Lin, Z. Wang, Z. Xi, X. Liu, Y. Xia, Theoretical models of ZnS nanoclusters and nanotubes: first-principles calculations, Solid State Commun. 147 (2008) 165–168.
[25] A. Al-Sunaidi, A. Sokol, C. Catlow, S. Woodley, Structures of zinc oxide nanoclusters: as found by revolutionary algorithm techniques, J. Phys. Chem. C 112 (2008) 18860–18875.
[26] B. Kaewruksa, W. Pipornpong, B. Wanno, V. Ruangpornvisuti, Density functional studies of small gases adsorbed on the ZnO sodalite-like cage and its adsorption abilities, Comput. Theor. Chem. 1020 (2013) 100–107.
[27] I. Sarsari, S. Hashemifar, H. Salamati, First-principles study of ring to cage structural crossover in small ZnO clusters, J. Phys.: Condens. Matter 24 (2012) 505502.
[28] B. Wang, S. Nagase, J. Zhao, G. Wang, Structural growth sequences and electronic properties of zinc oxide clusters $(ZnO)_n$ (n = 2–18), J. Phys. Chem. C 111 (2007) 4956–4963.
[29] B. Wang, X. Wang, G. Chen, S. Nagase, J. Zhao, Cage and tube structures of medium-sized zinc oxide clusters $(ZnO)_n$ (n = 24, 28, 36, and 48), J. Chem. Phys. 128 (2008) 144710.

[30] L. Ren, L. Cheng, Y. Feng, X. Wang, Geometric and electronic structures of $(BeO)_n$ (n = 2–12, 16, 20, and 24): rings, double rings, and cages, J. Chem. Phys. 137 (2012) 014309.

[31] A. Alexandrova, A. Boldyrev, H. Zhai, L. Wang, E. Steiner, P. Fowler, Structure and bonding in B_6^- and B_6: planarity and antiaromaticity, J. Phys. Chem. A 107 (2003) 1359–1369.

[32] M. Menon, E. Richter, A. Mavrandonakis, G. Froudakis, A. Andriotis, Structure and stability of SiC nanotubes, Phys. Rev. B 69 (2004) 115322.

[33] T. Oku, M. Kuno, H. Kitahara, I. Narita, Formation, atomic structures and properties of boron nitride and carbon nanocage fullerene materials, Int. J. Inorg. Mater. 3 (2001) 597–612.

[34] T. Oku, M. Kuno, I. Narita, Hydrogen storage in boron nitride nanomaterials studied by TG/DTA and cluster calculation, J. Phys. Chem. Solids 65 (2004) 549–552.

[35] T. Oku, A. Nishiwaki, I. Narita, M. Gonda, Formation and structure of $B_{24}N_{24}$ clusters, Chem. Phys. Lett. 380 (2003) 620–623.

[36] G. Seifert, P. Fowler, D. Mitchell, D. Porezag, T. Frauenheim, Boron–nitrogen analogues of the fullerenes: electronic and structural properties, Chem. Phys. Lett. 268 (1997) 352–358.

[37] S. Song, H. Chen, C. Zhang, G. Wang, Structures and bonding properties of $(BN)_n$ ($n \leqslant 12$) clusters, Acta Phys. Chim. Sin. 21 (2005) 735–739.

[38] D. Strout, Structure and stability of boron nitrides: isomers of $B_{12}N_{12}$, J. Phys. Chem. A 104 (2000) 3364–3366.

[39] D. Strout, Structure and stability of boron nitrides: the crossover between rings and cages, J. Phys. Chem. A 105 (2001) 261–263.

[40] A. Zobelli, C. Ewels, A. Gloter, G. Seifert, O. Stephan, S. Csillag, C. Colliex, Defective structure of BN nanotubes: from single vacancies to dislocation lines, Nano Lett. 6 (2006) 1955–1960.

[41] A. Aguado, J. Lopez, Structures and stabilities of CaO and MgO clusters and cluster ions: an alternative interpretation of the experimental mass spectra, J. Phys. Chem. B 104 (2000) 8398–8405.

[42] F. Bawa, I. Panas, Limiting properties of $(MgO)_n$ and $(CaO)_n$ clusters, Phys. Chem. Chem. Phys. 3 (2001) 3042–3047.

[43] G. Bilalbegovic, Structural and electronic properties of MgO nanotube clusters, Phys. Rev. B 70 (2004) 045407.

[44] E. De La Puente, A. Aguado, A. Ayuela, J. Lopez, Structural and electronic properties of small neutral $(MgO)_n$ clusters, Phys. Rev. B 56 (1997) 7607.

[45] R. Dong, X. Chen, X. Wang, W. Lu, Structural transition of hexagonal tube to rocksalt for $(MgO)_n$, $2 \leqslant n \leqslant 10$, J. Chem. Phys. 129 (2008) 044705.

[46] J. Goellner, K. Neyman, M. Mayer, F. Nortemann, B. Gates, N. Rosch, Ligand-free osmium clusters supported on MgO. A density functional study, Langmuir 16 (2000) 2736–2743.

[47] K. Kwapien, M. Sierka, J. Dobler, J. Sauer, M. Haertelt, A. Fielicke, G. Meijer, Structural diversity and flexibility of MgO gas-phase clusters, Angew. Chem. Int. Ed. 50 (2011) 1716–1719.

[48] C. Roberts, R. Johnston, Investigation of the structures of MgO clusters using a genetic algorithm, Phys. Chem. Chem. Phys. 3 (2001) 5024–5034.

[49] P. Sushko, J. Gavartin, A. Shluger, Electronic properties of structural defects at the MgO surface, J. Phys. Chem. B 106 (2002) 2269–2276.

[50] P. Ziemann, A. Castleman Jr., Stabilities and structures of gas phase MgO clusters, J. Chem. Phys. 94 (1991) 718.

[51] P. Ziemann, A. Castleman Jr., Mass-spectrometric study of the formation, evaporation, and structural properties of doubly charged MgO clusters, Phys. Rev. B 44 (1991) 6488.

[52] J. Xiang, X. Yan, Y. Xiao, Y. Mao, S. Wei, Structures and growth modes of $(TiO)_n$ ($n \leqslant 9$) clusters, Chem. Phys. Lett. 387 (2004) 66–69.

[53] G. Chen, Z. Liu, X. Gong, Structure and growth modes of $(BaO)_n$ ($n \leqslant 9$) clusters, J. Chem. Phys. 116 (2002) 1339–1342.

[54] J. Tao, J. Perdew, V. Staroverov, G. Scuseria, Climbing the density functional ladder: nonempirical metageneralized gradient approximation designed for molecules and solids, Phys. Rev. Lett. 91 (2003) 146401.

[55] D. Jiang, The expanding universe of thiolated gold nanoclusters and beyond, Nanoscale 5 (2013) 7149–7160.

[56] L. Cheng, B_{14}: an all-boron fullerene, J. Chem. Phys. 136 (2012) 104301.

[57] L. Cheng, J. Yang, Communication: new insight into electronic shells of metal clusters: analogues of simple molecules, J. Chem. Phys. 138 (2013) 141101.

[58] L. Li, L. Cheng, First principle structural determination of $(B_2O_3)_n$ (n = 1–6) clusters: from planar to cage, J. Chem. Phys. 138 (2013) 094312.

[59] R. Li, L. Cheng, Structural determination of $(Al_2O_3)_n$ (n = 1–7) clusters based on density functional calculation, Comput. Theor. Chem. 996 (2012) 125–131.

[60] Y. Yuan, L. Cheng, B_{14}^{2+}: a magic number double-ring cluster, J. Chem. Phys. 137 (2012) 044308.

[61] Y. Yuan, L. Cheng, Theoretical prediction for the structures of gas phase lithium oxide clusters:$(Li_2O)_n$ (n = 1–8), Int. J. Quantum Chem. 113 (2013) 1264–1271.

[62] G. Petersson, A. Bennett, T. Tensfeldt, M. Al-Laham, W. Shirley, J. Mantzaris, A complete basis set model chemistry. I. The total energies of closed-shell atoms and hydrides of the first-row atoms, J. Chem. Phys. 89 (1988) 2193–2218.

[63] P. Hay, W. Wadt, Ab initio effective core potentials for molecular calculations. Potentials for K to Au including the outermost core orbitals, J. Chem. Phys. 82 (1985) 299–310.

[64] A. McLean, G. Chandler, Contracted Gaussian-basis sets for molecular calculations. 1. 2nd row atoms, Z = 11–18, J. Chem. Phys. 72 (1980) 5639–5648.

[65] K. Schuchardt, B. Didier, T. Elsethagen, L. Sun, V. Gurumoorthi, J. Chase, J. Li, T. Windus, Basis set exchange: a community database for computational sciences, J. Chem. Inf. Model. 47 (2007) 1045–1052.

[66] P. Pyykko, N. Runeberg, Comparative theoretical study of N-heterocyclic carbenes and other ligands bound to Au, Chem.-Asian J. 1 (2006) 623–628.

[67] M. Frisch, G. Trucks, H. Schlegel, G. Scuseria, M. Robb, J. Cheeseman, G. Scalmani, V. Barone, B. Mennucci, G. Petersson, et al., Gaussian 09, Revision B. 01, Gaussian, Inc., Wallingford, CT, 2009.

[68] A. Panda, R. Behera, Comparative study of E···N (E = Se/Te) intramolecular interactions in organochalcogen compounds using density functional theory, J. Hazard. Mater. 269 (2014) 2–8.

[69] A. Alcock, H. Emeleus, A. Sharpe, Secondary bonding to nonmetallic elements, in: Advances in Inorganic Chemistry and Radiochemistry, vol. 15, Academic Press, 1972, pp. 1–58.

[70] W. Kabsch, C. Sander, Dictionary of protein secondary structure: pattern recognition of hydrogen-bonded and geometrical features, Biopolymers 22 (1983) 2577–2637.

[71] D. Zubarev, A. Boldyrev, Comprehensive analysis of chemical bonding in boron clusters, J. Comput. Chem. 28 (2007) 251–268.

[72] D. Zubarev, A. Boldyrev, Developing paradigms of chemical bonding: adaptive natural density partitioning, Phys. Chem. Chem. Phys. 10 (2008) 5207–5217.

[73] D. Zubarev, A. Boldyrev, Revealing intuitively assessable chemical bonding patterns in organic aromatic molecules via adaptive natural density partitioning, J. Org. Chem. 73 (2008) 9251–9258.

[74] E. Johnson, S. Keinan, P. Mori-Sanchez, J. Contreras-Garcia, A. Cohen, W. Yang, Revealing noncovalent interactions, J. Am. Chem. Soc. 132 (2010) 6498–6506.

[75] J. Contreras-Garcia, E. Johnson, S. Keinan, R. Chaudret, J. Piquemal, D. Beratan, W. Yang, NCIPLOT: a program for plotting noncovalent interaction regions, J. Chem. Theory Comput. 7 (2011) 625–632.

[76] T. Lu, F. Chen, Multiwfn: a multifunctional wavefunction analyzer, J. Comput. Chem. 33 (2012) 580–592.

[77] W. Humphrey, A. Dalke, K. Schulten, VMD: visual molecular dynamics, J. Mol. Graph. 14 (1996) 33–38.

[78] T. Sohnel, H. Hermann, P. Schwerdtfeger, Towards the understanding of solid-state structures: from cubic to chainlike arrangements in group 11 halides, Angew. Chem. Int. Ed. 40 (2001) 4381–4385.

[79] T. Sohnel, H. Hermann, P. Schwerdtfeger, Solid state density functional calculations for the group 11 monohalides, J. Phys. Chem. B 109 (2005) 526–531.

[80] P. Schwerdtfeger, P. Boyd, S. Brienne, J. McFeaters, M. Dolg, M. Liao, W. Eugen Schwarz, The mercury–mercury bond in inorganic and organometallic compounds. A theoretical study, Inorg. Chim. Acta 213 (1993) 233–246.

[81] H. Schmidbaur, The fascinating implications of new results in gold chemistry, Gold Bull. 23 (1990) 11–21.

[82] H. Schmidbaur, The aurophilicity phenomenon: a decade of experimental findings, theoretical concepts and emerging applications, Gold Bull. 33 (2000) 3–10.

[83] H. Schmidbaur, A. Schier, A briefing on aurophilicity, Chem. Soc. Rev. 37 (2008) 1931–1951.

[84] J. Martin, A. Sundermann, Correlation consistent valence basis sets for use with the Stuttgart–Dresden–Bonn relativistic effective core potentials: the atoms Ga–Kr and In–Xe, J. Chem. Phys. 114 (2001) 3408–3420.